Velocimetry analysis of type-I ELM precursors in ASDEX Upgrade

P. Manz[1,2], J.E. Boom[2], E. Wolfrum[2], G. Birkenmeier[2], I.G.J. Classen[3], N.C. Luhmann Jr.[4], U. Stroth[2,1] and the ASDEX Upgrade Team

[1] Physik-Department E28, Technische Universität München, James-Franck-Str. 1, 85748 Garching, Germany
[2] Max-Planck-Institut für Plasmaphysik, Boltzmannstr. 2, 85748 Garching, Germany
[3] FOM-Insitute DIFFER, Dutch Institute for Fundamental Energy Research, Association EURATOM-FOM, 3430 BE Nieuwegein, The Nederlands
[4] University of California at Davis, Davis, CA 95616, USA

Abstract. When the electron transport barrier remains in its final shape before a type-I ELM crash in ASDEX Upgrade, ELM precursors appear as electron temperature fluctuations. In order to relate these precursors to an instability, spatial scales, parity and the cross-phase between electron temperature and radial velocity fluctuations are evaluated by means of velocimetry of measured 2D electron temperature fluctuations. A comprehensive comparison with properties of different instabilities points to micro-tearing modes. Bispectral analysis indicates a nonlinear coupling of these precursors to a ballooning-type mode prior to the ELM onset.

1. Introduction

Edge localized modes (ELMs) lead to bursty quasiperiodic expulsions of energy and particles from the plasma edge into the scrape-off layer (SOL) in the state of high confinement (H mode) of magnetically confined fusion plasmas. ELMs are believed to be triggered by MHD instabilities, either the ideal peeling mode (IPM) or the ideal ballooning mode (IBM), depending on which stability boundary (the current or the pressure, respectively) is reached [1]. The ELM crash itself is a nonlinear phenomenon. The nonlinear drive is responsible of the explosive nature of MHD instabilities as observed as ELMs [2]. Linear simulations of peeling-ballooning modes predict high toroidal mode numbers n [3], while the experimentally observed structure are at low toroidal mode numbers [4, 5]. Nonlinear reduced MHD simulations can explain the growth of low n toroidal mode numbers by an inverse cascade mechanism [6, 7], which is a purely nonlinear feature. Furthermore nonlinear electromagnetic gyrokinetic simulations show that depending on $\beta = p/(B^2/2\mu_0)$ (with plasma pressure p and magnetic field strength B) different instabilities dominate the linear growth phase [8]. In the electrostatic regime, $\beta \leq 10^{-4}$, the ELM blowout is dominated by the ion temperature gradient mode (ITG). For values of large $\beta \geq 8 \cdot 10^{-4}$ a microtearing mode (MTM) grows and saturates by transferring its energy into more violent ITG MHD turbulence [8]. Thus also the MTM is a candidate for triggering ELMs. In between $10^{-4} \leq \beta \leq 8 \cdot 10^{-4}$ the ideal ballooning mode (IBM) takes over, resulting in a sharp increase in the ion heat transport followed by a rather slow decay of it. In simulations an explosive MHD behavior is not observed as nonlinear MHD processes are prevented by the fast turbulent energy transfer from the unstable MHD mode into the micro-turbulence. The growth of the MHD mode is stopped by nonlinear saturation and degradation of the initial temperature gradient.

Next the role of perturbations prior to the ELM called precursors is discussed. Following Ref. [9] the term precursor is used to denote perturbations that systematically precede ELMs, where the term trigger denotes rapidly growing perturbations prior to the ELM. Therefore ELM triggers are precursors, but precursors do not have to be triggers. In general precursors are associated with linear instabilities which do not necessarily lead to ELMs. Some precursors do not grow rapidly before the ELM, some show saturated amplitudes [9]. As they are not leading to ELMs, the question arises, why to study them? Precursors appear in situations, where the edge transport barrier remains in its final shape before an ELM crash. Therefore the linear instability conditions are similar for both precursors and ELM triggers. Thus, the investigation of ELM precursors can provide information on the linear instabilities, which most likely in a later phase interact nonlinearly to trigger the ELM. Therefore we will investigate the linear properties of the precursors (Sec. 5), before investigating the nonlinear coupling just prior to the ELM by a bispectral analysis (Sec. 7).

Experimentally ELM precursors are classified in low ($n \sim 1-3$) and high ($n \sim 5-15$) toroidal mode number precursors [9]. The lower n precursors are associated

with external kink (peeling) modes, the high n precursors show ballooning character [9]. This fits well in the peeling-ballooning paradigm and it also shows that as long as the modes do not strongly nonlinearly interact they cannot trigger the ELM and end up just as precursors. The linear instabilities of the precursors are the same which are associated with the ELM crash itself. In ASDEX Upgrade, ELM precursors of very high mode numbers have been observed [10]. These small structures are not expected to result from global MHD (peeling or ballooning or tearing) instabilities, but from micro-instabilities. In this work a comprehensive comparison of these precursors with different micro-instabilities is carried out and their role in the ELM triggering process through nonlinear coupling will be investigated. The features of the different instabilities are discussed in detail in Sec. 2. Already from the previous observations [10] it can be deduced that these precursors share very specific features with the microtearing mode. Here further evidence is provided by studying the cross-phase between pressure and potential fluctuations, which is one of the key quantities. Unfortunately, in high temperature plasmas in particular potential measurements are difficult to obtain and practically unavailable at the same temporal and spatial resolution as pressure fluctuations. Here, we deduce potential fluctuations $\tilde{\phi}$ from radial velocity fluctuations assuming $\tilde{v}_r = \tilde{E}_\theta/B = -\nabla_\theta\tilde{\phi}/B$ ($\tilde{E}_\theta$ is the poloidal electric field component) estimated by a velocimetry technique [11] from two-dimensionally measured electron temperature fluctuations $\tilde{T}_e$. The radial velocity fluctuations are chosen as those are not affected by a phase velocity and are given by the $E \times B$ velocity only due to gyroviscous cancellation [12]. This allows to estimate the cross-phase between $\tilde{\phi}$ and $\tilde{T}_e$ of type-I ELM precursors. As the strongest candidate for the precursor are microtearing modes, which are electromagnetic instabilities, the observed displacement via velocimetry could in principle also result from the fluctuations of the radial magnetic field. Fortunately, as discussed later in detail, the theoretically expected cross-phase between electron temperature fluctuations and fluctuations of the radial displacement either resulting from the $E \times B$-drift or from radial magnetic field fluctuations coincide for MTMs. Furthermore, the magnitude of the magnetic field fluctuations is estimated to be too small to be detected with the velocimetry technique. By a detailed comparison of propagation direction, size, cross-phase and parity other possible instabilities will be ruled out.

2. Instability characterization

It is possible that several instabilities (e.g. IPM, IBM, kinetic ballooning modes (KBM) [13], kinetic peeling ballooning modes (KPBM) [14], MTM, ITG, electron temperature gradient modes (ETG) [15]) are involved in the ELM cycle. In order to interpret the measured data, a characterization of the different instabilities is carried out (see Tab. 1). First, these instabilities can be distinguished by their characteristic size. The size is usually compared to the hybrid Larmor radius $\rho_s = \sqrt{m_i T_e}/(eB)$ with ion mass m_i, electron temperature T_e, elementary charge e and magnetic field strength B. Both IPM

Table 1. Properties of the linear instabilities ideal peeling mode (IPM), ideal and resistive ballooning mode ((I-R)BM), kinetic ballooning mode (KBM), kinetic peeling ballooning mode (KPBM), micro tearing mode (MTM), ion temperature gradient mode (ITG), trapped electron mode (TEM) and electron temperature gradient mode (ETG). The structures propagate either in electron (e dia.) or ion diamagnetic direction (i dia.) or do not have any preferential direction (n.p.). They have ballooning (ball.) or tearing (tear.) parity. Times are normalized to $L_\perp/c_s$, perpendicular spatial scales to ρ_s, where $L_\perp$ is the mean profile scale length, c_s is the sound speed, $\rho_s = \sqrt{T_e m_i}/eB$ with electron temperature T_e, ion mass m_i, magnetic field, elementary charge e and strength B.

Instability	drive	prop.	scale	$\alpha_{\phi,\tilde{p}}$	$\alpha_{\phi,\tilde{T}_e}$	$\omega(L_\perp/c_s)$	parity	Ref.
IPM	$J_\parallel$	n.p.	$k_\theta\rho_s \ll 0.1$				global	
(I-R)BM	∇p	n.p.	$k_\theta\rho_s < 0.1$	$\pi/2$			ball.	
KBM	$\nabla T_{e,i}$	i dia.	$k_\theta\rho_s \sim 0.1$	$\pi/2$			ball.	[13]
KPBM	$\nabla p_{e,i}$	e dia.	$k_\theta\rho_s \ll 0.1$				ball.	[14]
MTM	∇T_e	e dia.	$k_\theta\rho_s \sim 0.1$	0		0.1-1	tear.	[17, 18, 19]
ITG	∇T_i	i dia.	$0.1 < k_\theta\rho_s \leq 1$	$\pi/2$	π	0.1-1	ball.	[12, 19]
TEM	∇T_e,∇n	e dia.	$0.1 < k_\theta\rho_s$	0	$\pi/2$		ball.	[20]
ETG	∇T_e	e dia.	$k_\theta\rho_s > 1$	$\pi/2$	$0 - \pi/2$	0.5-100	ball.	[20, 19]

and IBM are long wavelength macro MHD instabilities and KBM, MTM, ITG and ETG are micro-instabilities appearing at much higher wave numbers and frequencies. KBM and MTM are of similar size ($k_\theta\rho_s \sim 0.1$ in a tokamak [19]) but are larger than the ITG mode ($0.1 \leq k_\theta\rho_s \leq 1$), which is still at much larger scales than the ETG [19]. The resistive counterpart of the IBM is the resistive ballooning mode (RBM), it appears at a similar scale ($k_\theta\rho_s \sim 0.1$ [12]) as the KBM and the MTM. In a spherical tokamak the MTM is closer to the ITG scale [16, 18]. But also for cold ions the MTM can reach smaller scales down to $k_\theta\rho_s \sim 0.5$ [19].

Second, the IPM and IBM can be distinguished by the stability limit. The current drives the IPM and the pressure the IBM, furthermore the IPM has lower toroidal mode numbers than the IBM.

Third, to distinguish the ballooning modes (I-RBM or KBM) from the MTM the cross-phase between pressure and potential fluctuations is needed. Those modes appear at similar wave numbers and frequencies. The RBM propagates with the background flow direction which should be small because ion diamagnetic and $E\times B$ flow compensate each other [21]. The MTM propagates in the electron diamagnetic direction. KBM and ITG also propagate in the same (ion-diamagnetic) direction. But as IBM, RBM and KBM are interchange modes the cross phase between potential and pressure fluctuations is close to $\pi/2$ [12]. Also the ITG is primarily an interchange instability. Hence the MTM can be distinguished by a small cross-phase and the propagation into the electron diamagnetic direction.

In the nonlinear situation also for pure ITG turbulence the cross-phase depends on the mechanism transferring the free energy $\tilde{p}^2$ to the field energy $\tilde{\phi}^2$. There are two possibilities [12]: first, the free energy can be transferred directly by the interchange effect $\tilde{p}\mathcal{K}\tilde{\phi}$ due to the curvature $\mathcal{K}$. The curvature operator $\mathcal{K} \sim ik_\theta$ induces a phase shift of $\pi/2$. Second, the energy is transferred via the magnetic energy $\tilde{J}_\parallel^2$ by adiabatic $\tilde{J}_\parallel \nabla_\parallel \tilde{p}$ and Alfvénic coupling $\tilde{J}_\parallel \nabla_\parallel \tilde{\phi}$. If the first mechanism is dominant the modes are more interchange-like, if the second is dominant the modes are drift-wave like with a cross-phase between $\tilde{\phi}$ and $\tilde{p}$ close to zero [12]. Due to the nonlinear vorticity advection the high wavenumber, high frequency regime can be expected to be drift-wave dominated, whereas the low wavenumbers should be dominated by the linear instabilities [12].

In the following the connection of MTMs with drift-waves is discussed in more detail. Including electron and ion gradient drifts in the tearing instability results in drift-tearing modes [22]. The governing equations [17] include the evolution of the magnetic flux ψ

$$\frac{1}{c}\frac{d}{dt}\psi = -\eta_\parallel J_\parallel + \frac{T}{ne}\nabla_\parallel n + \frac{\hat{\alpha}}{e}\nabla_\parallel T, \tag{1}$$

the vorticity $\nabla^2\phi$

$$\frac{d}{dt}\nabla^2\phi = 4\pi(\frac{v_A^2}{c^2})\nabla_\parallel J_\parallel, \tag{2}$$

the density n

$$\frac{d}{dt}n = \frac{1}{e}\nabla_\parallel J_\parallel, \tag{3}$$

and the electron temperature T_e

$$\frac{d}{dt}T_e = \frac{2}{3}\hat{\alpha}(\frac{T_e}{ne})\nabla_\parallel J_\parallel + D_\parallel \nabla_\parallel^2 T_e, \tag{4}$$

where c is the speed of light, $\eta_\parallel$ the plasma resistivity, $\hat{\alpha}$ the Braginskii thermal force coefficient, v_A is the Alfvén velocity and $D_\parallel = T/\eta_\parallel ne^2$. Those equations include the basic drift-wave dynamics (Eqs. (2) and (3)). The change in the magnetic flux ψ associated with a magnetic island is usually accompanied by a parallel current $J_\parallel$. This also follows from Ampère's law $J_\parallel = -(c/4\pi)\nabla^2\psi$. If this parallel current exhibits a finite toroidal mode number also a parallel variation of the parallel current is likely $\nabla_\parallel J_\parallel \neq 0$ and the divergence in the parallel current couples density, temperature and vorticity fluctuations. Therefore magnetic perturbations can transfer the free energy to the fluctuating fields via adiabatic and Alfvénic coupling and a vanishing cross-phase between pressure and potential fluctuations can be expected. In this sense a tearing mode leads to drift-wave-like dynamics of the turbulence. Of course also the magnetic fluctuations associated with the MTM can result in a radial displacement of the temperature fluctuations.

As the MTM is related to magnetic islands it induces a magnetic field fluctuation $\tilde{B}_x$ resulting in a displacement of the plasma which would be interpreted by the velocimetry as a radial velocity. Finally the expected cross-phase relation between this displacement and the electron temperature fluctuations has to be discussed. For micro-tearing modes

the radial magnetic fluctuations $\tilde{B}_x$ are in phase with the fluctuations in the radial temperature gradient $\frac{d\tilde{T}_e}{dx}$ [23], and thus it is out of phase with the electron temperature fluctuations themselves. Therefore for a MTM with a drift-wave like cross-phase we can expect the same phase behavior between radial velocity and electron temperature fluctuations regardless whether the $E \times B$ drift or magnetic islands are responsible for the radial displacements from which the velocity fluctuations are deduced.

Forth, for the MTM in order to generate magnetic stochasticity the parity with respect to the magnetic vector potential is important [23]. In an up-down symmetric tokamak eigenmodes are characterized by their either tearing (even) or ballooning (odd) parity with respect to the magnetic vector potential $\tilde{A}_\parallel$. ITGs and TEMs exhibit ballooning parity, where $\tilde{A}_\parallel$ is zero at the resonance surface. MTMs exhibit tearing parity and can create magnetic islands, break field lines and create a stochastic magnetic field. Assuming the magnetic perturbations localized at the outboard midplane, the electrostatic potential of MTMs would exhibit an up-down asymmetry around the midplane and the corresponding radial $E \times B$ velocity fluctuations have a maximum around the midplane.

The different mode characterizations summarized in Tab. 1 will be tested experimentally in Sec. 4 and 5.

3. Experimental setup and previous investigations on ASDEX Upgrade

Experiments were carried out on the ASDEX Upgrade tokamak, which has major and minor horizontal radii of $R_0 = 1.65\,\mathrm{m}$ and $a = 0.5\,\mathrm{m}$, respectively. The ELM recovery cycle has been investigated in Ref. [15]. After the ELM crash temperature and density stay low for about 1–2 ms, then after a short increase the electron temperature stagnates while the density starts to increase. The final recovery of the temperature starts 4–5 ms after the ELM crash [15]. Electron temperature gradient modes (ETGs) were suggested as a possible candidate to explain the stagnation of the temperature gradient.

Two different types of ELM cycles can be distinguished in ASDEX Upgrade. So-called fast ELMs are triggered immediately after the recovery from the ELM crash, and so-called slow ELMs exhibit an extended phase where the electron transport barrier remains in its final shape before the ELM crash occurs [15]. For the latter precursors are observed in the electron temperature fluctuations [10].

A typical type I ELMy H-mode plasma (# 24793) is studied here, which was previously analysed in Ref. [10]. Electron temperature fluctuations $\tilde{T}_e$ were measured with a 2D imaging (ECEI) diagnostic [24]. The ECEI diagnostic consists of an array of 16 detectors, out of which 12 have been used for the present study. Each of the detectors acts as a 1D ECE radiometer measuring the intensity of the electron cyclotron radiation from different vertical positions in second harmonic X-mode (100–140 GHz). 16 lines of sight are focused on the low-field side plasma edge. Per line of sight 8 local oscillator frequencies allow measurements on 8 different radial positions. The radial resolution is 1.36 cm, where four channels per LOS measure inside the last-closed flux surface

and four channels in the scrape-off layer (SOL). The sampling rate of the diagnostic was 200 kHz. The ECEI is calibrated against the 1D-ECE diagnostic sharing the same viewing window. Details on the diagnostic can be found in Ref. [24]. The calibration and the influence of decreasing optical thickness are discussed in Ref. [10] for the presented discharge.

The plasma current was $I_p = 1$ MA, the magnetic field strength was $B = -2.5$ T at an edge safety factor of $q_{95} = 4.7$. The plasma parameters were $T_e = 500$ eV, $T_i = 700$ eV (measured at $R = 2.1$ m), core line-integrated electron density $\bar{n}_e = 8 \cdot 10^{19}$ m^{-3}. The density and electron temperature profiles prior to the ELM of the same discharge analysed here can be found in Fig. 3 of Ref. [10]. 7 MW of neutral beam injection and 750 kW of electron cyclotron resonance heating were applied. More details on the discharge are given in Ref. [10].

There are two types of precursors. The first type, called off-midplane fluctuations, do not trigger the ELM crash [10]. These off-midplane fluctuations appear about 2 ms before the ELM crash in the range of 20–50 kHz at poloidal mode numbers $m = 112 \pm 12$ and toroidal mode numbers $n = 28 \pm 7$. The modes are observed with a poloidal size of about 10 cm at the outboard midplane. Since in a non-circular cross-section of a flux-surface in X-point configuration the poloidal angle θ does in general not have the same direction as the derivative of the poloidal magnetic field, the size has to be corrected by the ratio to the poloidal angle in straight field line approximation θ^* ($d\theta/d\theta^* \approx 3.65$). Therefore the poloidal wavelength of the off-midplane fluctuations is about 3 cm in straight field line approximation.

The thermo-current in the outer divertor is used as an indicator for the occurrence of ELMs. The start time of the ELM is defined as the transcendence of a predefined offset value. The ELM is triggered about 200 μs before the actual ELM onset by fluctuations with mode numbers $m = 74 \pm 9$ and $n = 18 \pm 4$ [10]. These pertubations are the second kind of ELM precursors and are called ELM triggers, here. For both, off-midplane fluctuations and ELM triggers, the temperature fluctuations propagate into the electron diamagnetic direction [10].

4. Velocimetry results

As the fluctuations are two-dimensionally resolved the velocity field can be estimated via velocimetry, where sections of two consecutive images are compared for similar structures. The displacement of the structures gives the velocity field. Velocimetry has been widely used for the interpretation of gas-puff-imaging data [25, 26, 27, 28, 29]. The technique avoids misinterpretation due to tilted structures in the plasma edge present in the standard time delay estimation approach to estimate the velocity [30]. Here the radial propagation velocity of turbulent structures has been estimated with a rather simple particle image velocimetry (PIV) algorithm optimized for noisy data [11], including a pattern matching technique, subpixel interpolation and denoising by removing displacement vectors which seem quite different from any of their neighboring

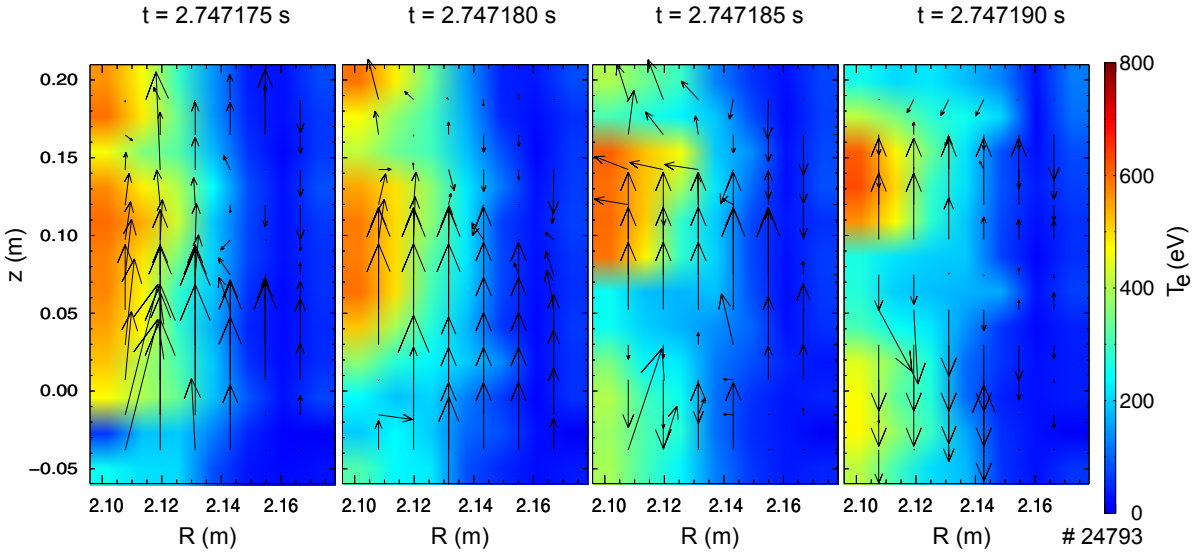

Figure 1. Four panels in the consecutive frames (with 5 μs temporal resolution) showing the T_e evolution just prior the ELM crash at 2.7472 s. A mode is propagating in electron diamagnetic direction. Arrows show the velocimetry results, which are showing a mostly poloidal propagation.

displacements.

A limit to the minimum changes of the temperature that can be resolved with ECE is given by the noise in the black body radiation emitted from the plasma [31]. The r.m.s noise level is set by $\tilde{T}/T = \sqrt{\Delta f_\nu / \Delta f_{RF}}$, where f_{RF} is the receiver bandwidth (100-140 GHz) and f_ν is the bandwidth at which the video is recorded (200 kHz). This gives a detection limit of 0.1 %. To investigate the effect of noise on the velocimetry algorithm it has been applied to synthetic data with a noise level of 2 % and could clearly recover the motion of the predefined mode. To gain further confidence in the velocimetry algorithm, it has also been applied to data from a turbulence simulation and could recover the optical flow of plasma blobs, even though not at ELM relevant parameters.

Figure 1 shows an example of four panels in consecutive frames (with 5 μs temporal resolution) showing the T_e evolution just prior to the ELM crash at 2.7472 s (see Fig. 3). A mode is propagating in electron diamagnetic direction. Arrows represent the velocimetry results, which show a mostly poloidal propagation. Estimated radial velocity fluctuations for three inner channels are shown in Fig. 2a–c with a zoom for the inner most channel in Fig. 2d. As the radial velocity is estimated by comparing the frame before the actual one with the frame after the actual one, the velocity is basically estimated in units of px/2frames = 1.36 cm/10 μs =1.36 km/s. The radial displacement is up to one pixel in phases where the off-midplane fluctuations are present and up to two pixels directly before the ELM crash. For the off-midplane fluctuations specific features at the inner most radial positions are found. The radial velocity takes its maximum around the midplane ($z = 0$ cm), which is consistent with a strong decrease of the plasma

potential around the midplane. Above the midplane negative velocity fluctuations are found, which is consistent with an increase in the plasma potential. Consistent with low radial velocity fluctuations in between those two positions the plasma potential takes its minimum above the midplane. As the plasma potential decreases at the midplane, there is also a maximum below the midplane. This points to an up-down asymmetry in the radial velocity fluctuations and to tearing parity of the potential fluctuations. This feature is restricted only to the innermost channels ($\rho = 0.94$), further outwards ($\rho = 0.97$ and $\rho = 0.99$) the radial velocity is always outwards directed, without this characteristic asymmetry. The fluctuations directly prior to the ELM crash do also show an asymmetry in the radial velocity, this is also restricted to the innermost position ($\rho = 0.94$), but their appearance is poloidally shifted with respect to the off-midplane fluctuations. In simulations of the inter-ELM evolution of the pedestal on a spherical tokamak, also tearing parity modes are found close to the pedestal top and ballooning parity modes in the pedestal [32, 33].

5. Cross-phase analysis

In order to distinguish between the different instabilities, the cross-phase between plasma potential and pressure fluctuations is the key quantity. Assuming that the radial propagation velocity of the fluctuations is due to $E \times B$ advection, the potential was deduced from the velocity field. We correlate the obtained potential field with the electron temperature fluctuations. As the ELM cycle is very dynamic and inherently non-stationary we favor the wavelet transformation of electron temperature and radial velocity fluctuations, which provides the frequency information for every point of the time series. The wavelet transform is given by

$$T(t) \rightarrow T_f(t) = \int d\acute{t}\psi(f(t-\acute{t})T(\acute{t}) \tag{5}$$

where the Morlet wavelet

$$\psi(t) = C(e^{i2\pi t} - e^{-2\pi^2})e^{-t^2/2} \tag{6}$$

is used here. The wavelet auto spectrum is then given by

$$S_T(t,f) = \langle T_f^*(t)T_f(t)\rangle, \tag{7}$$

where the asterisk denotes the complex conjugate and $\langle\cdot\rangle$ is the ensemble average. The spectra $T_f^*(t)T_f(t)$ are calculated for the four inner channels for every line of sight. Afterward the data is averaged over the ensemble of all 48 channels. The temporal sequence of off-midplane fluctuations, ELM trigger and ELM is shown in Fig. 3. The divertor current shown in Fig. 3a indicates the ELM onset. Figure 3b shows the wavelet auto spectrum of the electron temperature fluctuations in a logarithmic representation. The off-midplane fluctuations as studied in Ref. [10] appear around 2.761 s in the range of 20–40 kHz. Before the ELM onset, marked by the vertical line, broadband fluctuations are observed.

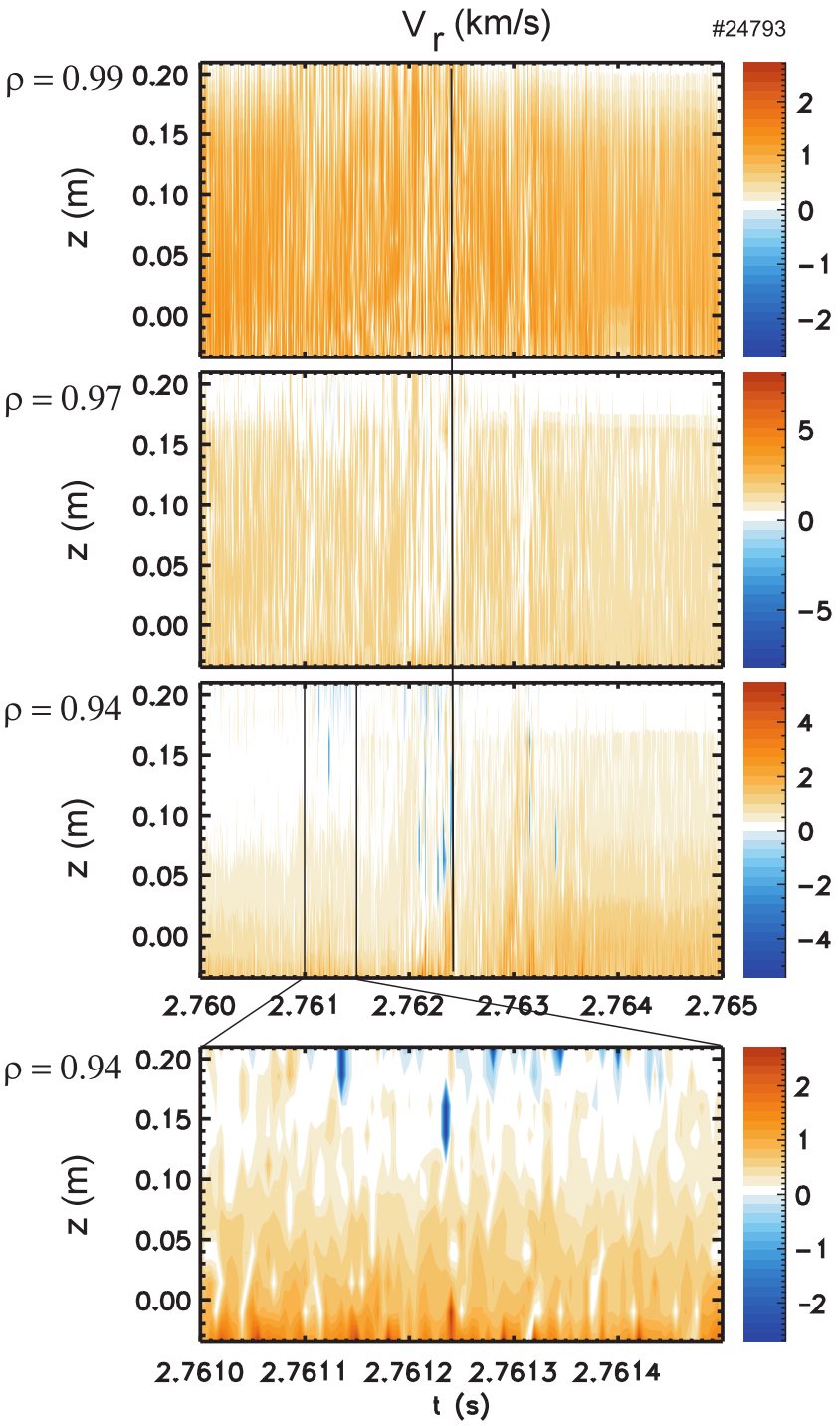

Figure 2. Radial velocity fluctuations for the three inner channels in units of km/s. The solid black line denotes the ELM onset.

The wavelet cross spectrum between two poloidally separated channels $T_{\theta 1}(t)$ and $T_{\theta 2}(t)$, given by

$$S_\theta(t, f) = \langle T^*_{\theta 1 f}(t) T_{\theta 2 f}(t) \rangle, \tag{8}$$

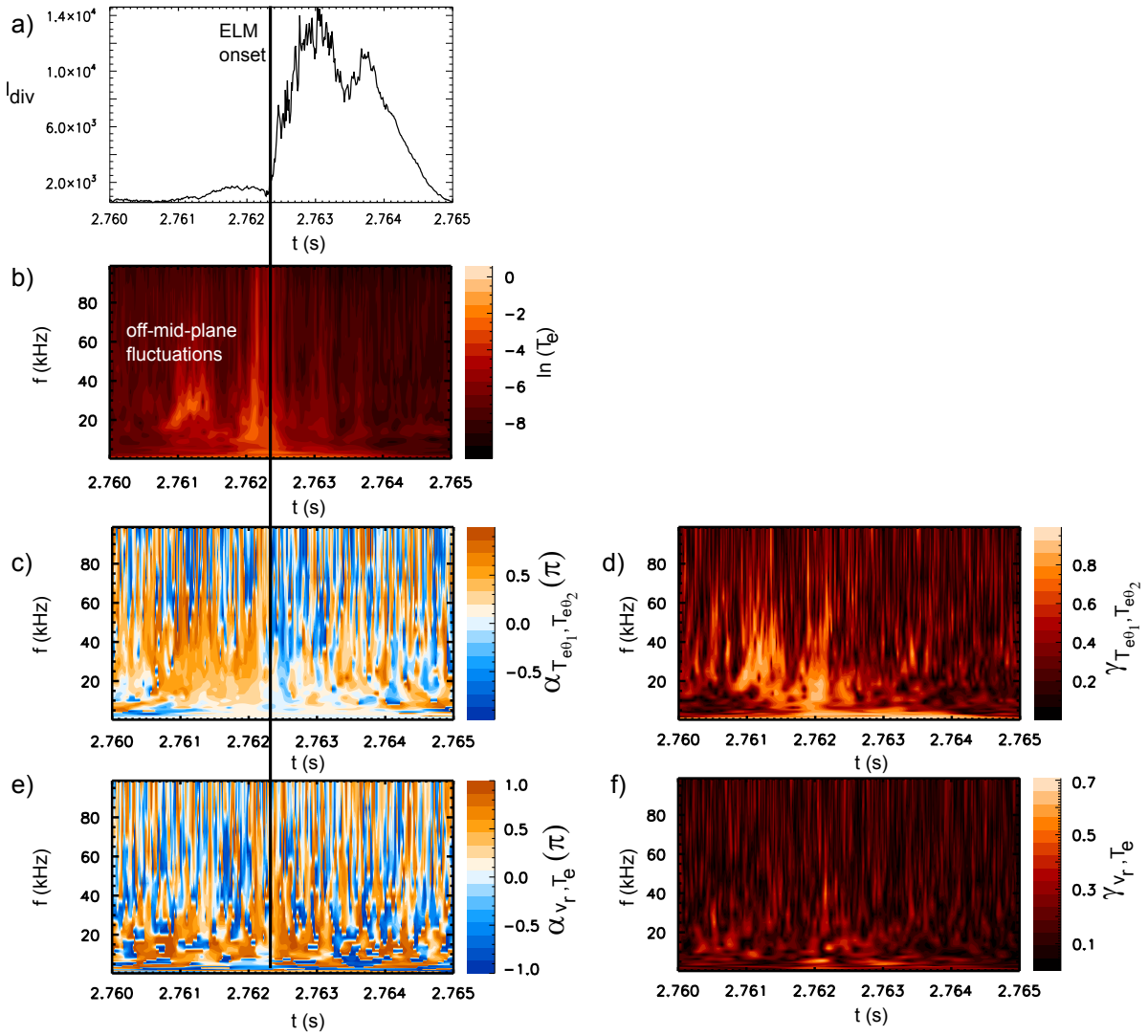

Figure 3. (a) Divertor current, (b) wavelet auto spectrum of electron temperature fluctuations in linear frequency dependence and an arbitrary logarithmic intensity scale (the dark region show low intensity), (c) cross-phase and (d) coherency between poloidally separated channels, (e) cross-phase and (f) coherency between electron temperature and radial velocity fluctuations. The phases are shown in units of π.

can be used to estimate the propagation direction of a distinct frequency mode. As we already know the propagation direction this is a consistency test. This complex quantity can be represented by its amplitude and its phase. The amplitude is called cross-coherence

$$\gamma_{S_\theta(t,f)} = \frac{\|S_\theta(t,f)\|}{\sqrt{S_{T_{\theta 1}}(t,f) S_{T_{\theta 2}}(t,f)}}, \tag{9}$$

which measures how phase-locked the modes at a frequency f in the two signals are. It gives values between zero and one. The phase is the cross-phase $\alpha_{T_{\theta 1}, T_{\theta 2}}$. A positive cross-phase represents a positive time lag and therefore the present choice of poloidally separated channels indicates propagation in the electron-diamagnetic direction. The

cross-phase is shown in Fig. 3c. As observed in Ref. [10] and consistent with the velocimetry results both the off-midplane fluctuations and the fluctuations at the ELM onset propagate in the electron diamagnetic direction. See also the details of the off-midplane fluctuations and the fluctuations at the ELM onset as shown in Figs. 4 and 5, respectively.

The significance of the results is given by the cross-coherence. It is compared against the $\alpha = 95\%$ confidence limit given by $(1 - (1 - \alpha)^{\frac{1}{1-M}})$, where M is the number of realisations in the ensemble [34]. The number of realisations is given by 11 realisations taken at four radial locations. That gives an ensemble of 44 and the results are significant, if the cross-coherence strongly exceeds 0.07. The cross-coherence for the off-midplane fluctuations as well as for the fluctuations at the ELM onset exceeds 0.9 (Fig. 3d). As the ensemble does not consist only of independent measurements, however the number of independent realisations is much smaller in reality.

Interestingly the frequency range above 50 kHz shows more activity in the ion-diamagnetic direction (blue color in Fig. 3c) shortly before and after the ELM, which is similar to the observations of KBMs in DIII-D [13]. However, this particular frequency range is not well resolved by the ECEI system. The amplitude is low as seen in Fig. 3a and also the cross-coherence is low (0.05–0.3 shown in Fig. 3d) in our analysis and this observation is not significant.

The wavelet cross spectrum between temperature and radial velocity fluctuations is given by

$$S_{Tv_r}(t, f) = \langle T_f^*(t) v_{rf}(t) \rangle \tag{10}$$

where the cross-phase α_{T_e,v_r} of $S_{Tv_r}(t, f)$ is close to zero for interchange modes and close to $\pi/2$ for drift waves. The cross-phase is shown in Figs. 3e, 4b and 5b. Both, the off-midplane fluctuations (Fig. 4b) and the fluctuations at the ELM onset (Fig. 5b) have a cross-phase around $\pi/2$ pointing to drift waves. The cross-coherence for the modes is quite different, 0.3 for the off-midplane fluctuations (Fig. 4c) and 0.7 for the fluctuations at the ELM onset (Fig. 5c). These are compared with the 95% confidence limit for the 33 realisations given by 0.1. As the velocimetry does not provide velocity estimates of the boundary the ensemble consists of 11 poloidal measurements with three radial positions each. Hence, the results are significant.

The difference in the cross-coherence levels between the offmid-plane fluctuations and the actual ELM precursor are due to the corruption of the velocimetry results at the edge of the observation region, where the off-midplane fluctuations are most prominent. It should be noted, however, that a cross-phase of $\pi/2$ is observed for every of the about 20 ELM precursor fluctuations analysed. As these fluctuations do not show interchange characteristics (a cross phase of zero between radial velocity and temperature fluctuations) IBMs, KBMs, linear ITGs and ETGs can be ruled out. The drift-wave nature of the fluctuations together with the up-down asymmetry of the amplitudes point to micro-tearing modes (MTMs). Also the strong similarity to perturbations observed at higher collisionalities during type-II ELMs in ASDEX

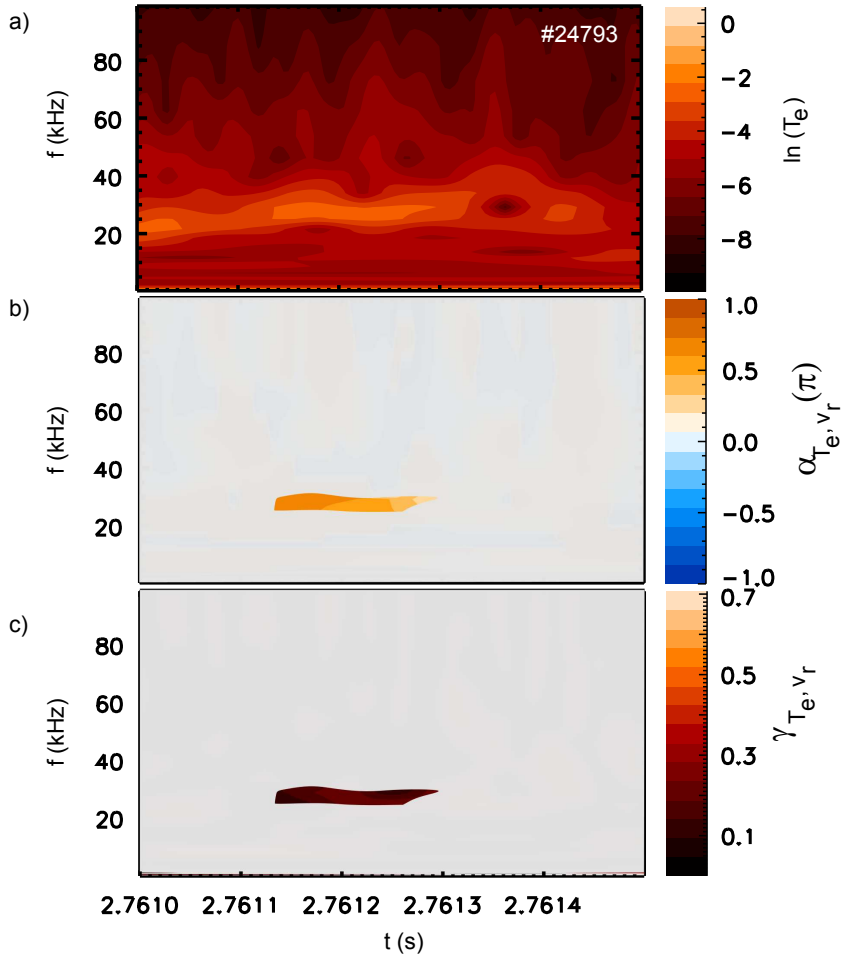

Figure 4. (a) Wavelet auto spectrum of electron temperature fluctuations, (b) cross-phase and (c) coherency between temperature and radial velocity fluctuations of the off-midplane fluctuations not triggering the ELM. The data is shown in the same representation as in Fig. 3, but to guide the eye the cross-phases at small intensities are shaded.

Upgrade [44] points to tearing modes. Those are accompanied by a flattening of the temperature profile characteristic for magnetic islands.

6. Additional support for microtearing modes

The background values (Sec. 3) correspond to a $\rho_s \approx 1.3$ mm. At the pedestal top $\beta \approx 2 \cdot 10^{-3}$, which is clearly above the electron ion mass ratio m_e/m_i and therefore electromagnetic effects are important. The pedestal top is in high β conditions, where MTMs can trigger ELMs [8]. Around the separatrix $\beta \approx 3 \cdot 10^{-4}$, which points to ballooning modes responsible for the ELM blowout.

Together with $\rho_s \approx 1.3$ mm we obtain $k_\theta \rho_s \approx 0.3$, which is of the order as predicted for MTMs ($k_\theta \rho_s \sim 0.1$). The expected frequency of MTMs in slab geometry is given by

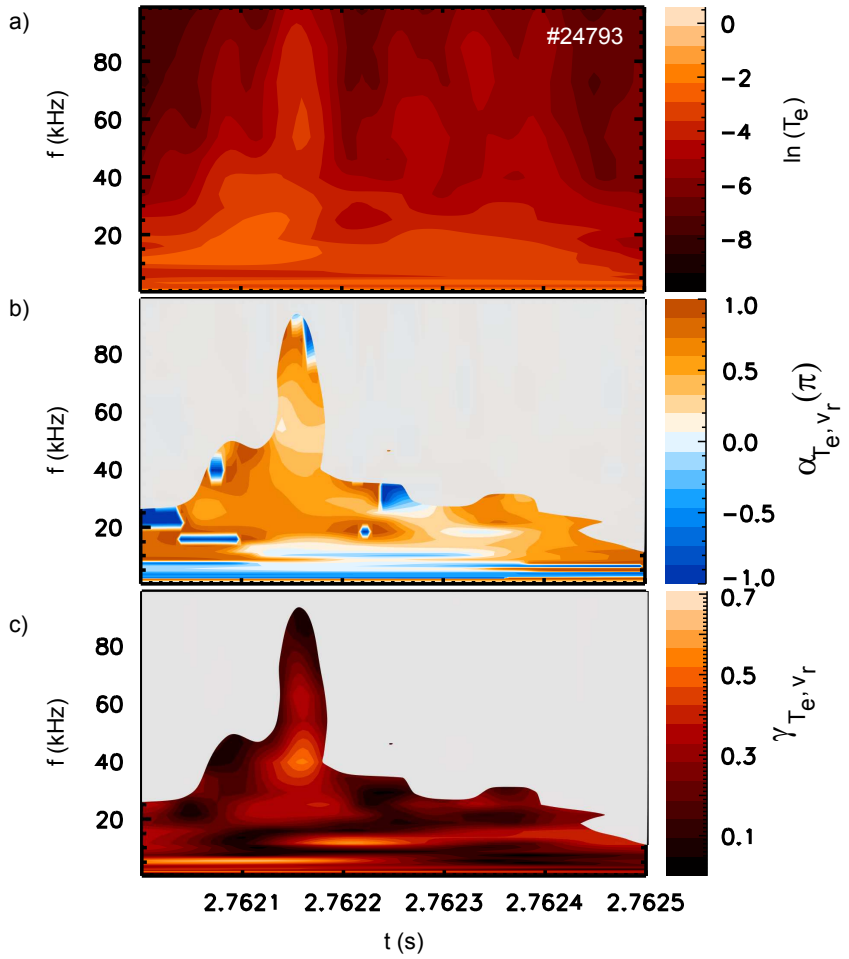

Figure 5. (a) Wavelet auto spectrum of electron temperature fluctuations, (b) cross-phase and (c) coherency between temperature and radial velocity fluctuations of temperature fluctuations prior to the ELM onset. The data is shown in the same representation as in Fig. 3, but to guide the eye the cross-phases at small intensities are shaded.

[35]

$$\omega = \frac{5}{4} k_\theta \rho_e v_{te} \frac{1}{L_{Te}} \tag{11}$$

where $\rho_e = \sqrt{2 m_e T_e}/eB$ is the electron Larmor radius, $v_{te} = \sqrt{2T_e/m_e}$ the electron thermal velocity v_{te}. We have neglected the contribution from the density gradient to the electron diamagnetic drift as it is close to be flat at the pedestal top. From the electron temperature profile we estimate the electron temperature fall-off length $L_{T_e} = T_e/\nabla T_e \approx 1/8$ m, which gives an estimated frequency for MTMs of 146 kHz taking the poloidal wavenumber in straight field line approximation or 40 kHz in the local (slap corresponding) approximation. The expected level of magnetic fluctuations for MTMs can be estimated by $\tilde{B}_x/B \sim \rho_e/L_{T_e} \approx 6 \cdot 10^{-4}$ [36]. The stochastic field created by these magnetic fluctuations would lead to a displacement of $\Delta x = (\tilde{B}_x/B) L_c \approx 1.2$ mm, which is close to the ion Larmor radius ρ_i (with the correlation length $L_c = \pi q R \sim 20$ m) [23].

The estimated displacement velocity $\Delta v = \Delta x/\Delta t \approx 80$ m/s with $\Delta t = L_c/v_{te}$ [23] is much smaller than the velocimetry detection limit of 1.36 km/s. The radial displacement due to magnetic fluctuations is too small to dominate the velocimetry results.

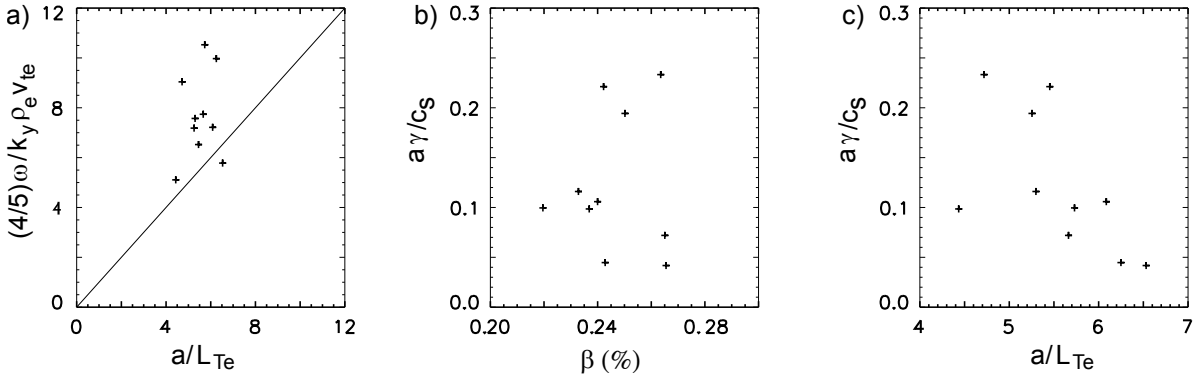

Figure 6. Dispersion relation (a) and growth rate dependent on β (b) and electron temperature fall-off length (c).

To further support the MTM as the responsible linear instability of the off-midplane fluctuations the scaling of the frequency and the growth rate with L_{Te} and β is investigated. The electron temperature fall-off length L_{Te} and β are estimated by the averaged values during the offmid-plane fluctuations at the pedestal top. It has to be noted that the L_{Te} scalings (Figs. 6a and c) are not at constant β and the β scaling (Fig. 6b) is not at constant L_{Te}. The frequency of the off-midplane fluctuations is close to the value predicted by Eq. (11) for MTMs, but does not show any trend (Fig. 6a). The growth rate is estimated by the e-folding length of the fluctuation amplitude at the onset of the off-midplane fluctuations as done in Ref. [37]. The growth rates tend to decrease with the electron temperature gradient (Fig. 6c). As MTMs are driven by the electron temperature gradient, this seems to be inconsistent with the MTM. However, as discussed in Ref. [38] the growth rate of MTMs does not show a monotonic dependence on a/L_{Te} in general. At this high values of $a/L_{Te} > 3 - -4$ the growth rate decreases, before a transition to KBMs may occur [38]. Due to the a/L_{Te} dependence the growth rate decreases with β for $\beta \geq 0.26$ % (Fig. 6b) after an increase with β for $\beta \leq 0.26$ %.

7. Identification of the ELM trigger

If now the off-midplane fluctuations and the actual ELM precursors are both MTMs, the question arises, why do the off-midplane fluctuations not trigger the ELM directly and the other fluctuations do or at least correlate with the triggering process. One difference is that the ELM trigger appears on all frequencies (as shown in Fig. 3b at 2.762 s and Fig. 5) which is quite unnatural for a linear instability. During a nonlinear coupling process, however, a linear unstable mode f_{lin} with a low frequency mode f_{low} sidebands $f_{lin} \pm f_{low}$ are excited. These sidebands than can couple with the low frequency mode to $f_{lin} \pm f_{low} \pm f_{low}$ and so forth. Such a coupling chain may generate the observed

broadband feature of the ELM. The low frequency mode can be a different linear instability. And indeed a low frequency mode at about 5–10 kHz is observed only before the ELM is triggered (Fig. 3 at 2.762 s and Fig. 5) and is not observed, when the off-midplane fluctuations do not result in an ELM (Fig. 3 at 2.761 s and Fig. 4).

Whether the perturbations prior to the ELM actually lead to the ELM is speculative. It is also possible that the MTM prevents the ELM onset and it is its disappearance prior to the ELM, which allows the pressure gradient to rise leading to the ELM. Snyder et al. proposed a ELM suppression model, where an island at the pedestal top blocks the inward expansion of the pedestal width in the recovery region [45]. Further evidence for the importance of mode coupling can be obtained from nonlinear analysis.

The bicoherence provides information on the nonlinear coupling between different modes. It is given by

$$b^2(t, f_1, f_2) = \frac{\|\langle T_{f_1}(t) T_{f_2}(t) T^*_{f_1+f_2}(t)\rangle\|^2}{\langle\|T_{f_1}(t) T_{f_2}(t)\|^2\rangle\langle\|T^*_{f_1+f_2}(t)\|^2\rangle}. \tag{12}$$

The bicoherence measures how phase-locked modes are with values in [0,1], which is a requirement for nonlinear interaction. The integrated bicoherence is shown in Fig. 7a. For both precursors a higher integrated bicoherence is found, indicating intensified nonlinear activity. In both cases also low frequency modes are nonlinearly active. During the off-midplane fluctuations as shown in Fig. 7b the nonlinear coupling is dominated by coupling of the off-midplane fluctuation at $f_2 = -25$ kHz with its second harmonic $f_1 \approx 50$ kHz ((A) in Fig.7b). As the second harmonic does not appear in the power spectrum itself, it suggests that the second harmonic is damped representative of a nonlinear saturation process. At the same time all frequencies couple to the $f_2 = \pm 1$ kHz ((B) in Fig. 7b), which is similar to the coupling with a zonal flow [39, 40]. This coupling likely corresponds to the nonlinear saturation via energy transfer to the sheared (zonal) flow, often termed as shear suppression. However the direction of the energy transfer cannot be deduced from the bispectrum itself and this observation could be particularly interesting in respect of the investigation in Ref. [41], where it is shown that the nonlinear excitation of MTMs by zonal flows is responsible for the magnetic stochasticity. Also a strong coupling between the $f_2 = \pm 10$ kHz with modes above $f_1 > 60$ kHz is observed.

In the case of the ELM triggering event (Fig. 7c), the 20 kHz fluctuations also couple with their higher harmonics ((A) in Fig. 7c) and a low frequency modulation ((B) in Fig. 7c) is observed, but the coupling to the zonal flow (A) is weaker. The main difference is a strong coupling of the 20 kHz mode with a 5 kHz mode ((C) in Fig.7c). The 5 kHz mode may receive energy from the MTM and thus grow to be the trigger instability of the ELM (fluctuations appearing on all scales). The interaction of this mode with all frequencies represents the modulation of the turbulent fluctuations by this mode. As seen in Figs. 3 and 5 this mode appears with a cross-phase between temperature and radial velocity fluctuations close to zero and shows interchange character. Therefore this might be the ballooning mode expected to be responsible for the ELM formation. The

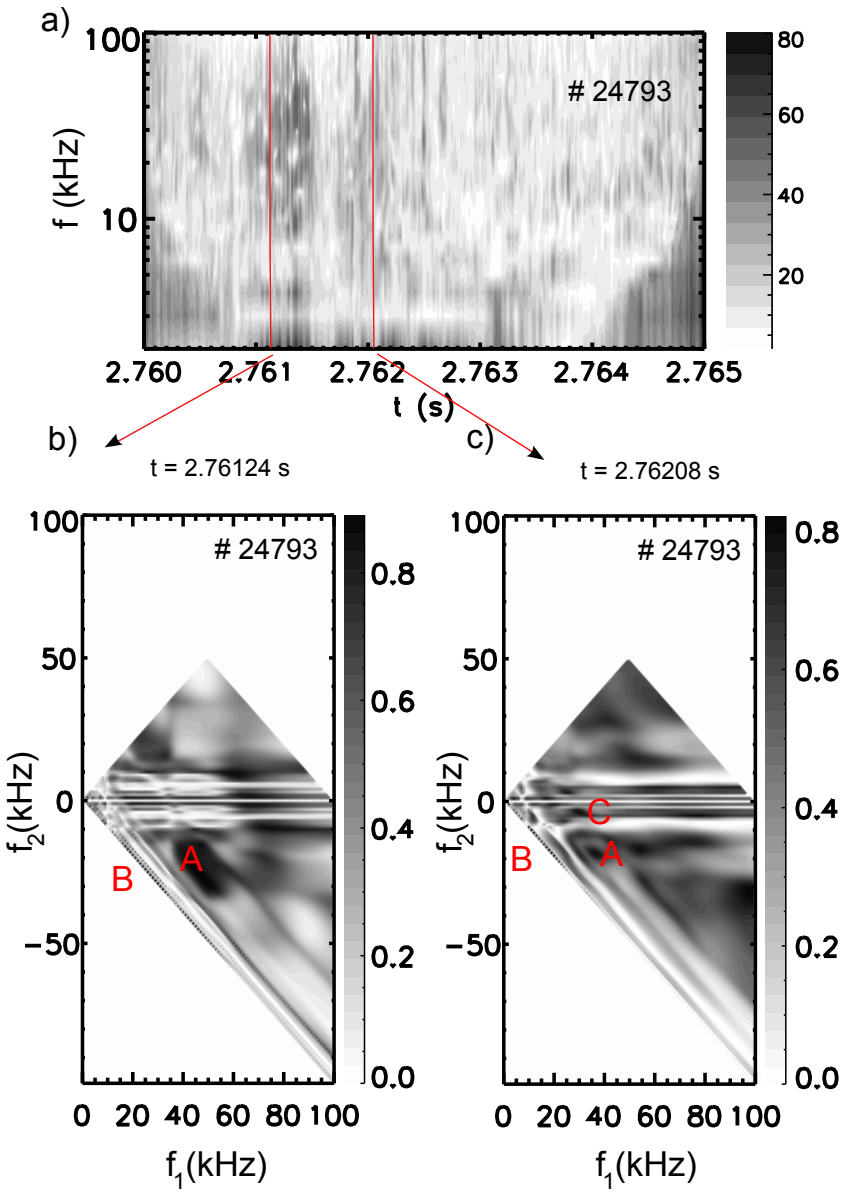

Figure 7. a) Integrated bicoherence (here the frequency is shown in a logarithmic scale, the dark regions show strong bicoherence), b) bicoherence during the off-midplane fluctuations and c) the actual ELM trigger.

ELM filament might result from a coupling of both modes, the 5 kHz (ballooning-like) and the 20 kHz (tearing-like) mode.

8. Discussion and Summary

During type-I ELM cycles in ASDEX Upgrade with a low repetition rate temperature fluctuations appear as precursors just prior to the ELM crash. Similar temperature fluctuations appear also as off-midplane fluctuations about 2 ms before the ELM crash. In both phases the electron temperature fluctuates in the range of 20–50 kHz with

poloidal mode numbers of $m = 112 \pm 12$ and toroidal mode numbers of $n = 28 \pm 7$ [10]. Up to now no instability could be assigned to these fluctuations. Due to their poloidal wavelength in the order of $k_\theta \rho_s \sim 0.1$ ideal or kinetic ballooning modes or microtearing modes are strong candidates. In general the cross-phase between potential and pressure fluctuations is a key quantity to distinguish different instabilities in a plasma. Here two-dimensionally resolved electron temperature fluctuations have been used to estimate the radial propagation velocity via velocimetry. The cross-phase between radial velocity fluctuations and electron temperature fluctuations is close to $\pi/2$, which points to a drift-wave nature of these modes. This excludes ballooning modes from being responsible for these fluctuations. On the other hand, several features point to microtearing modes:
(i) The fluctuations occur at poloidal wave numbers in the order of $k_\theta \rho_s \sim 0.1$, this is a turbulent length scale and rules out neoclassical tearing modes which are usually observed at much lower mode numbers.
(ii) The fluctuations propagate in electron-diamagnetic direction.
(iii) The off-midplane character of the fluctuations is strongly characteristic for micro-tearing modes and not expected for pure drift waves.
(iv) The radial velocity and therefore the potential fluctuations point to a tearing parity and lead to the fact that the electron temperature fluctuations have their maximum off the midplane.
(v) These fluctuations show a cross-phase between radial velocity and temperature fluctuations close to $\pi/2$.
Most other modes, which are discussed with respect to plasma edge stability and turbulence, can be excluded either by size (IPM, KPBM, ETG), propagation direction (KBM, ITG) or cross-phase (IBM, RBM, KBM, linear ITG, TEM) (see Tab. 1). In general also small neoclassical tearing modes (at the scale of MTMs) would be consistent with the presented results.
What appears odd with the expectations for MTMs is the radial extent of the fluctuations. Micro-tearing modes are expected to be radially localized with radial wavelengths close to or smaller than the ion Larmor radius $\rho_i \approx 2$ mm. The observed temperature fluctuations appear at a much larger scale. However, a fine structure not detected due to the rather poor radial resolution (1.6 cm) cannot be excluded. Furthermore, the tearing parity is only observed at the innermost position ($\rho = 0.94$). This leads to the conclusion that only around that position the mode is a tearing mode. The observed large radial extent and the appearance as a coherent mode may be explained as follows: Microtearing modes exhibit radially much wider magnetic field perturbations [42] than density or potential perturbations. These magnetic field perturbations can induce resistive drift-waves at the outer edge. As resistive drift wave turbulence is subcritical [43] the turbulence can lock to magnetic field perturbations induced by the tearing mode. Therefore resistive drift-wave turbulence appears on the observed large scale as a coherent mode. An additional fine structure is of course not to be excluded.

The further important observation is that ballooning-like modes (with a cross-phase

close to zero) are found to appear at lower frequencies (around 5 kHz) together with the precursors, when the ELM is triggered. A study of the bicoherence shows that these modes satisfy the three-wave coupling condition and presumably couple nonlinearly to the MTMs at 20 kHz prior to the ELM. Thus, the MTM can transfer energy to the otherwise stable ballooning mode and makes it grow. The excited ballooning mode can then tap energy from the background gradient itself. However, by the energy transfer to the ballooning mode the MTM may be suppressed allowing an otherwise blocked inward expansion of the pedestal width [45]. The modulation of the tearing mode due to ballooning may explain the poloidal displacement of the tearing parity of the precursor fluctuations with respect to the off-midplane fluctuations, where this nonlinear coupling is absent. The results suggest that both the magnetic reconnection and stochasticity capabilities of tearing modes as well as the strong instability and transport capabilities of ballooning modes are needed to trigger ELMs.

Acknowledgements

The authors thank H. Doerk, C. Angioni, E. Fable and K. Lackner for fruitful discussions.

References

[1] Wilson H R, Cowley S C, Kirk A, Snyder P B, 2006 *Plasma Phys. Control. Fusion* **48** A71
[2] Wilson H R, Cowley S C, 2004 *Phys. Rev. Lett.* **92** 175006
[3] Snyder P B et al, 2009 *Nucl. Fusion* **49** 085035
[4] Wenninger R P et al, 2012 *Nucl. Fusion* **52** 114025
[5] Wenninger R P et al, 2013 *Nucl. Fusion* **53** 113004
[6] Hölzl M et al, 2012 *Phys. Plasmas* **19** 082505
[7] Krebs I, Hölzl M, Lackner K, Günter S, 2013 *Phys. Plasmas* **20** 082506
[8] Kendl A, Scott B D, Riberio T T, 2010 *Phys. Plasmas* **17** 072302
[9] Perez C P et al, 2004 *Nucl. Fusion* **44** 609
[10] Boom J E et al, 2011 *Nucl.Fusion* **51** 103039
[11] Crocker J C, Grier D G, 1996 *J. Colloidal Interface Sci.* **179** 298
[12] Scott B D, 2005 *Phys. Plasmas* **12** 062314
[13] Yan Z et al, 2011 *Phys. Plasmas* **18** 056117
[14] Wan W et al, 2012 *Phys. Rev. Lett.* **109** 185004
[15] Burkhart A et al, 2010 *Plasma Phys. Control. Fusion* **52** 105010
[16] Diallo A et al, 2013 *Phys. Plasmas* **20** 012505
[17] Scott B D, Drake J F, Hassam A B, 1985 *Phys.Rev. Lett.* **54** 1027
[18] Guttenfelder W et al, 2012 *Phys. Plasmas* **19** 056119
[19] Told D et al, 2008 *Phys. Plasmas* **16** 055901
[20] Görler T, Jenko F, 2008 *Phys. Rev. Lett.* **100** 185002
[21] Viezzer E at al, 2012 *Rev. Sci. Inst.* **83** 103501
[22] Drake J F, Lee Y C, 1977 *Phys. Fluids* **20** 1341
[23] Doerk, H 2012 *Ph.D thesis, Universität Ulm*
[24] Classen I G J at al, 2010 *Rev. Sci. Inst.* **81** 10D929
[25] Munsat T, Zweben S J, 2006 *Rev. Sci. Inst.* **77** 103501
[26] Sechrest Y et al, 2012 *Nucl.Fusion* **52** 123009

[27] Cziegler I et al, 2013 *Phys. Plasmas* **20** 055904
[28] Myra J R at al, 2013 *Nucl. Fusion* **53** 073013
[29] Xu G S et al, 2014 *Nucl.Fusion* **54** 013007
[30] Fedorczak N et al, 2012 *Phys. Plasmas* **19** 122302
[31] Suttrop W, Peeters A G, 1997 *IPP Report* 1/306
[32] Dickinson D et al, 2011 *Plasma Phys. Control. Fusion* **53** 115010
[33] Dickinson D et al, 2012 *Phys. Rev. Lett.* **108** 135002
[34] Manz P, Ramisch M, Stroth U, 2010 *Phys. Rev. E* **82** 056402
[35] Gladd N T, Drake J F, Chang C L, Liu C S, 1980 *Phys. Fluids* **23** 1182
[36] Drake J F, Gladd N T, Liu C S and Chen C L, 1980, *Phys. Rev. Lett.* **44** 994
[37] Manz P et al, 2012 *Phys. Plasmas* **19** 072311
[38] Moradi S et al, 2013 *Nucl.Fusion* **53** 063025
[39] Manz P, Ramisch M, Stroth U, 2009 *Phys. Rev. Lett.* **103** 165004
[40] Xu M et al 2012 *Phys. Rev. Lett.* **108** 245001
[41] Hatch D et al, 2012 *Phys. Rev. Lett.* **108** 235002
[42] Guttenfelder W et al, 2011 *Phys. Rev. Lett.* **106** 155004
[43] Manz P et al, 2011 *Plasma Phys. Control. Fusion* **53** 095001
[44] Boom J E et al, 2012 *Nucl.Fusion* **52** 114004
[45] Snyder P B et al, 2012 *Phys. Plasmas* **19** 056115